Proceedings World Geothermal Congress 2010
Bali, Indonesia, 25-29 April 2010

Geologic and Geomechanical Reservoir Simulation Modeling of High Pressure Injection, West Salak, Indonesia

Keita Yoshioka[1] and Jim Stimac[2]

1. Chevron Energy Technology Company, 1500 Louisiana, Houston TX 77002, USA
2. Chevron Geothermal Salak, Sentral Senayan II Office Tower 26th Fl, Jl. Asia Afrika No. 8, Jakarta 10270, Indonesia

e-mail: yoshk@chevron.com, jstimac@chevron.com

Keywords: injection, well stimulation, geomechanics, reservoir characterization.

ABSTRACT

Awi 18-1 is an injection well drilled in the Cianten Caldera, near the western margin of the Salak (Awibengkok) reservoir in west Java, Indonesia. The initial well injectivity was low, so long-term hydraulic stimulation was conducted to improve the permeability and establish a better connection to existing natural fractures. A reservoir geologic model of the area was built by integration of surface mapping, log and core data, and well performance information.

The well penetrated pre- and post-caldera volcanics, the caldera ring fault intrusion and contact metamorphic zone, and marine sedimentary rocks. Permeability was found primarily near the caldera margin in pre-caldera lavas and ring fault intrusion along steeply dipping NNW to NE-trending fractures that were partially sealed by mineral precipitation.

A simulation model was developed from the reservoir geologic model to understand the injectivity evolution mechanisms and behaviors under different injection conditions, and also predict long term future injectivity performance using the Geo-Mechanical Reservoir Simulator (GMRS®). The model contains the completed interval of deviated Awi 18-1 and the model domain covers the majority of microseismic events observed during the course of the stimulation. It simulates injectivity evolution using heat and mass transfer in an elastic formation.

The model was history-matched by calibrating rock mechanical and fracture properties. A number of what-if operational scenarios were simulated to evaluate the effects on injection rate of injection pressure and temperature, well shut-ins, and injectate temperature variation. In the numerical experiments, better performance was observed through higher pressure and lower injection temperature. Temperature cycling or periodic well shut-ins temporarily increase the injectivity but the stimulated volume (created fracture volume) is simply proportional to the amount of the volume injected and its temperature.

1. INTRODUCTION

Wells were drilled to the west of the Salak field from 2006 to 2008 to delineate the potential of the area for deep injection. Awi 17-1 and 18-1 were drilled within Cianten Caldera, and Awi 20-1 was drilled just outside the inferred southeastern caldera boundary (Figure 1). The well permeability in this area is low, and a campaign of hydraulic stimulation was employed to improve their performance. This paper describes the geologic model of the area based on the results of drilling and testing of these wells, and a geomechanical model of Awi 18-1 injectivity based on geologic model and measured and inferred rock properties. It also summarizes actual well improvement through the course of hydraulic stimulation efforts.

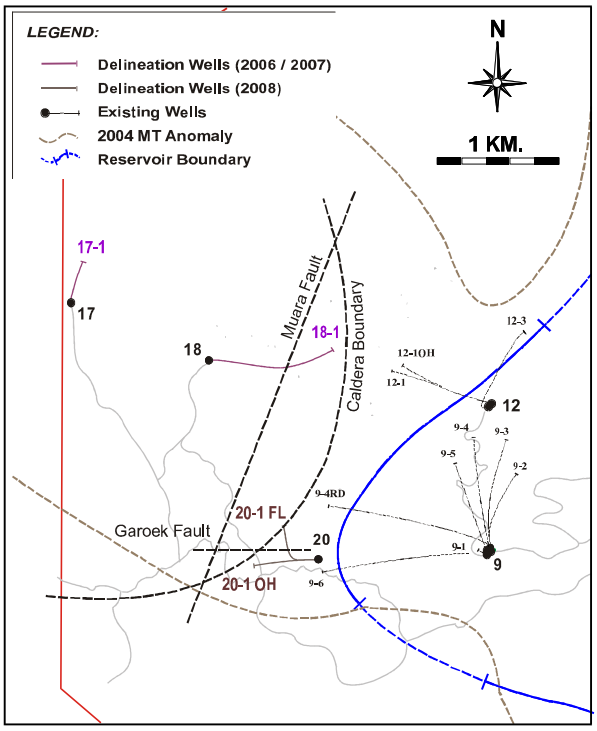

Figure 1: Map of Salak geothermal reservoir showing Awi 18-1, offset wells, and main geologic elements influencing well results in the area.

1.1 Background Geology and Well Stratigraphy

The Cianten caldera collapsed ≤670,000 years ago, and has subsequently been partially filled by post-caldera lavas, and sedimentary deposits and tuffs (Stimac et al., 2008). Surface structures cutting post-caldera units show prominent N to NE (0-50°) and NW (330-340°) trends (Stimac et al., 2010). The most important structures in the Awi 18-1 area are the caldera ring fault and Muara fault. The less prevalent NNW to NW and E-W fractures are more common in the older rocks, however one young E-W fault was observed near Awi 20-1. The area is thought to have a normal stress regime, with a maximum horizontal stress oriented NNE (approximately 24°; Sugiaman, 2003).

The Muara and Cianten faults appear to have localized erosion and eventual breaching of the caldera wall in the northeast, where the Cisaketi River and its tributaries now drain it and the northwestern portion of the Salak geothermal field (Figure 1).

2. DRILLING AND GEOLOGIC CONSTRAINTS

Awi 18-1 was drilled with full returns, providing a good understanding of the stratigraphy and alteration encountered (Figure 2). Additionally cores and logs were taken to provide data on fracture and rockmass properties. The well was targeted directionally to cut the caldera sequence and penetrate the eastern caldera ring fault. Inside the caldera it encountered a sequence of post-caldera sedimentary rocks and tuffs, caldera-related tuffs, and underlying pre-caldera andesitic to basaltic rocks that comprise the ancestral cone and underlying volcanic sequences. Submarine volcanism is evidenced by basaltic to andesitic hyaloclastite and lava interbedded with limestone and siliciclastic rocks bearing marine fossils. The caldera wall was encountered at about 7620 ft MD (3836 ft bsl), where a thick hypabyssal dacite porphyry intrusion, contact metasedimentary rocks, and microdiorite to diorite intrusions were drilled. The well exited the intrusion and contact zone at 9320 ft MD (5226 ft bsl), and reached its deepest point at 9642 ft MD (5598 ft bsl) in marine siliciclastic rocks.

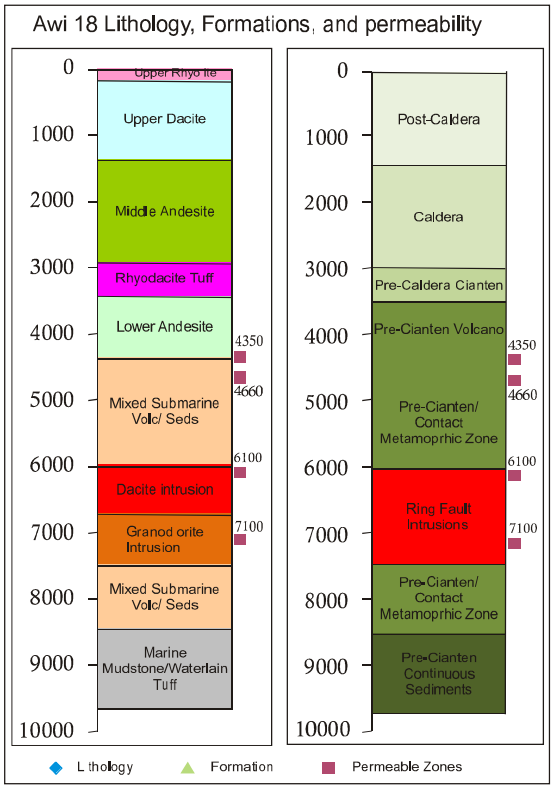

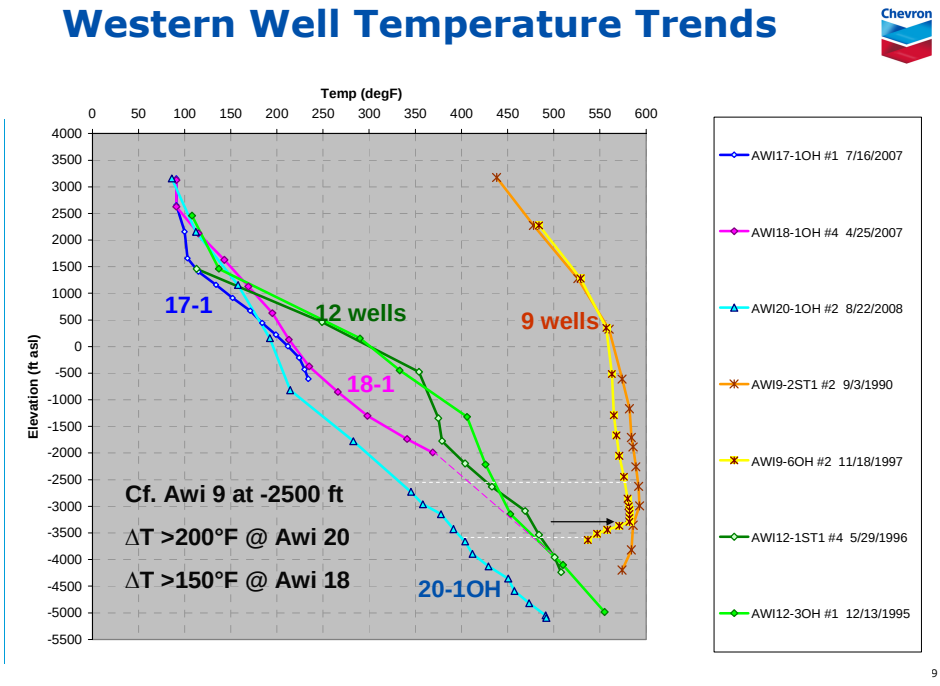

Figure 2: Awi 18-1 lithology, formations, and permeable zones (top), with depth in ft MD, and static formation temperature with elevation (ft rsl) relative to nearby wells (bottom).

The well had a conductive temperature gradient measured to about 2000 ft bsl after heat-up, similar to other far western wells (Awi 17-1, 20-1, 12-1). Nearby Awi 9 wells wells have convective gradients and much higher temperatures (Figure 2).

2.1 Fracture and rock mass properties

Cores of andesitic lava and breccia, and dacite porphyry intrusion were tested for mechanical properties, and a dipole shear sonic log was also run in the 12-1/4" hole section. These data, along with complementary data from offset wells provide constraints for geomechanical simulation of the well's response to injection. Mechanical properties used in the simulation are listed in Table 1.

Based on resistivity formation image log (XRMI) interpretation, clusters of open and partially open steeply dipping fractures were mapped from about 3300 to 7700 ft MD, or 172 to 3902 ft bsl (Figure 3). These fracture trends, along with fluid losses during drilling, and a PTS log described below indicate that initial permeability was primarily along NNW to NE-striking fractures (Figure 3), favorably oriented for failure relative to current stress field (Sugiaman, 2003).

Table 1: Rock properties and number of elements.

Model TVD ft	# of Element	Lithology	Elastic (Mpsi)	Poisson's ratio	Density (g/cc)
3440-4615	16800	Andesite/Dacite	6.5	0.3	2.57
4615-4656	1400	Basalt	8.5	0.31	2.5
4656-4730	1400	Rhyolite	9	0.31	2.77
4730-5152	7000	Dacite	7	0.3	2.55
5152-5352	2800	Limestone	5	0.32	2.58
5352-5544	2800	Andesite	6	0.32	2.53
5544-6200	9800	Limestone w/ some dacite	7.5	0.31	2.64
6200-6965	11200	Dacite/Andesite	9.5	0.28	2.45
6965-9440	23800	Unknown	9.5	0.28	2.45
9440-13440	11200	Unknown	9.5	0.28	2.45

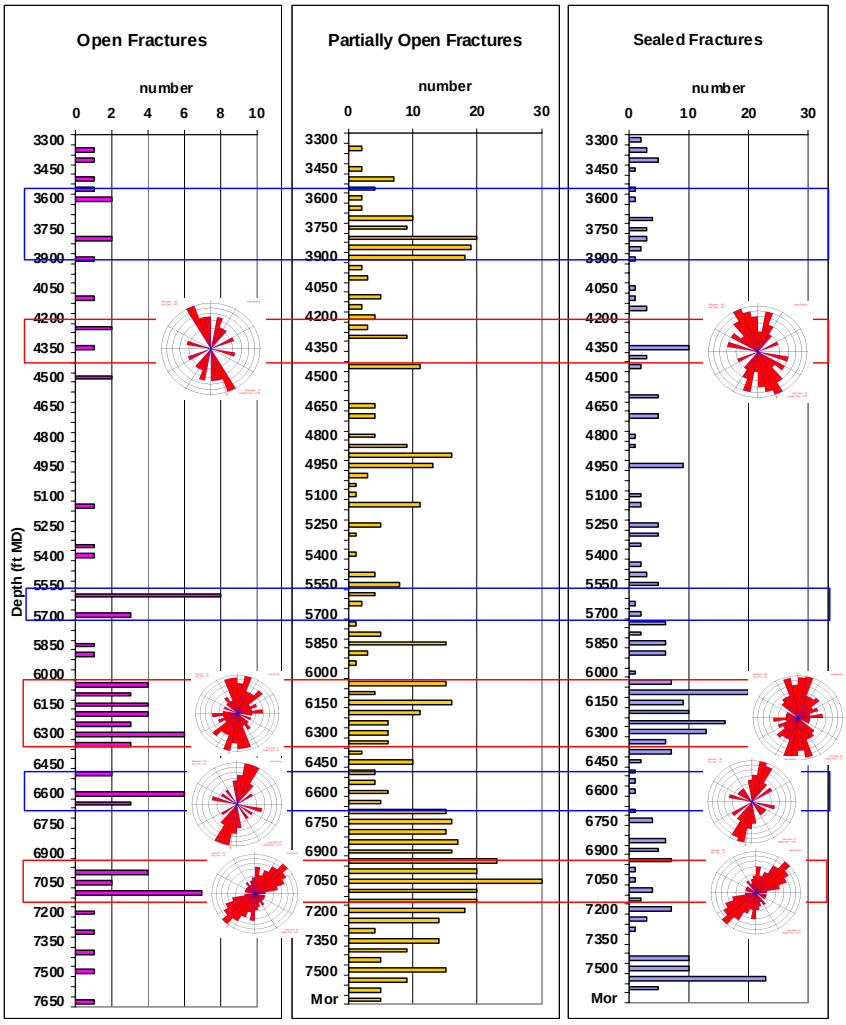

Figure 3: Histograms of fracture density with depth (50 ft intervals) and fracture strike for open + partially open (left side) and all (right side) for intervals that were modeled. Interpreted permeable zones in red boxes.

2.2 Microseismicity

Microseismicity was associated with hydraulic stimulation at injection wellhead pressures >600 psia. The shallowest microearthquake events associated with hydraulic stimulation were at about 3600 to 3940 ft bsl. This is deeper than the inferred permeable zones, probably due to uncertainties in the velocity model being used. However, the microearthquake locations suggest that fractures at 6100 ft MD (2636 ft bsl) or deeper were opened during the early stages of hydraulic stimulation, and that these and other fractures were stimulated at progressively deeper levels mostly the Cianten caldera (Wibowo and Nordquist, 2010).

3. WELL INJECTION HISTORY

3.1 Pre-stimulation measurements

Based upon the well completion test, the initial injectivity index (II) of Awi 18-1 was 0.45 kph/psi, below expectations (Yoshioka *et al.*, 2009). Figure 4 shows the results from a step-rate injection test. It indicates that the II improves as the injecting wellhead pressure is increased.

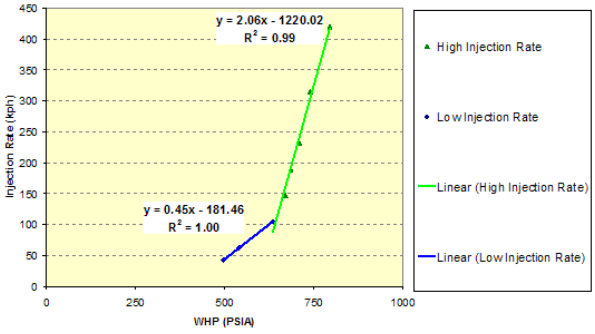

Figure 4: Injectivity test results.

The injectivity index (II) is defined as:

$$II = \frac{q_{inj}}{p_{wf} - p_r} \qquad (1)$$

where q_{inj} is the injection rate, and p_{wf} and p_r are the pressure of bottomhole and reservoir respectively. The II can be computed from the slope of injection rate – wellhead pressure curve. If a significant frictional pressure drop is expected, the wellhead pressure needs to be corrected to the proper bottomhole pressure value. The point where the injectivity trend changes slope is understood to be the fracture opening or extension pressure.

The fracture extension pressure found from injectivity test in geothermal wells would be different from what is considered as in oil and gas field. Due to its significant temperature difference induced during the injectivity test, the stress field could largely alter from the in-situ condition. Also, since the well is completed over a large interval (>6000 ft), the fracture opening would be a certain number of events at multiple points rather than the entire interval or single zone.

A PTS log conducted under 20 bpm injection indicates that 34% of the injected mass is taken at the 4350-4660 ft MD (1170-1443 ft bsl; Figure 5). Due to an obstruction in the 8-5/8" liner, the tool could not pass below 6100 ft MD (2636 ft bsl). The remaining of 64% of injected mass exits the well below this depth. Partial losses encountered at 6120 ft MD (2652 ft bsl) during drilling indicate a permeable zone at this depth. The fracture extension pressure can be read from the injectivity test (Figure 4) as about 650 psi. Therefore, we can back-calculate the bottomhole pressure at 4350 ft MD applying the well pressure gradient of 0.4 psi/ft as 2390 psi (= 650 + 0.4*4350). The minimum stress gradient for Salak is estimated as 0.54 psi/ft (Sugiaman, 2003), thus the stress at 4350 ft MD (4289 ft TVD) can be estimated as 2316 psi (=0.54*4289), which reconciles with the fracture extension pressure at the surface.

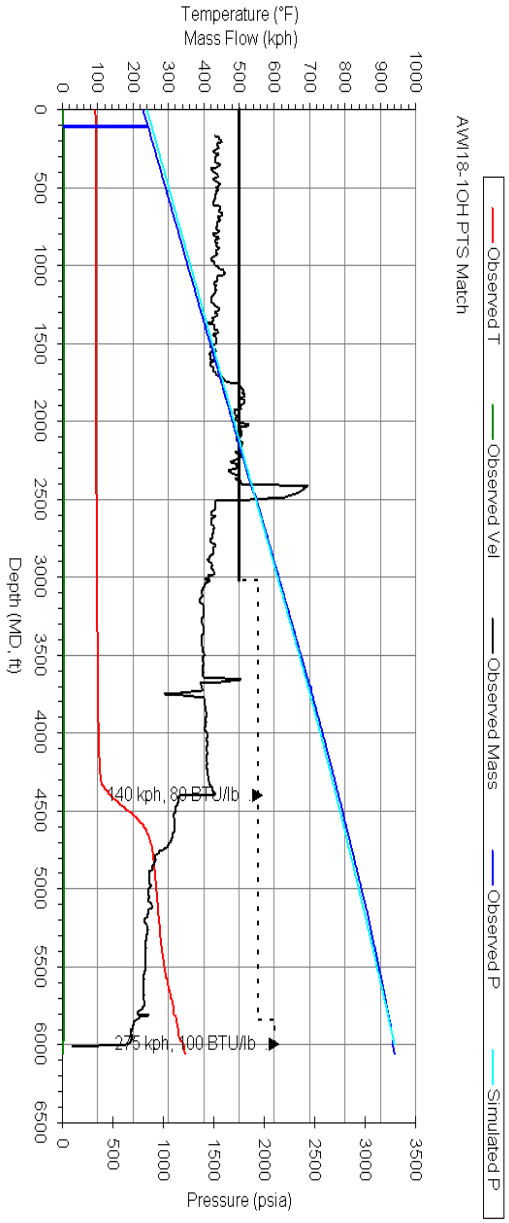

Figure 5: PTS under 20 bpm injection.

3.2 A long term water injection stimulation

Considering the past successes on hydraulic stimulation on other tight wells in Salak, a long term water injection was chosen as a stimulation method. The first phase injection stimulation was conducted from May 8 to August 22, 2007 (Figure 6). The results show lower WHP than before the stimulation, indicating conductivity improvements of existing fractures and/or newly development of tensile fractures around the wellbore.

Given the success observed in injectivity improvement by the first phase water injection, the second phase of injection

was started on Oct 31, 2007. The injection was stopped on Aug 26, 2008 and the pressures have been measured until Sep 19. Figure 7 shows the injection rate and WHP of the second phase injection stimulation.

Figure 7 shows a general trend of declining WHP and increasing injection rate with time, but both the decline of WHP and rise in injection rate are greater earlier on and level off later. Overall the injectivity of Awi 18-1 increased more than 150 % (3x) after the long term cold water injection.

4. SIMULATION OF INJECTION

The stimulation owes its success to the longer period of injection and lower temperature injectate, whereas the impacts from wellhead pressure and cycling-pressure type injection remain uncertain. To be able to address these impacts is extremely important since the duration of pump usage is the main cost of a stimulation project. An optimal usage of surface facility is then desired for stimulation design.

To shed light on the permeability enhancement mechanisms, a geomechanical reservoir simulator that is capable of reproducing the permeability changes by fracture growth over the long period, is desired. A similar attempt has been made in past using a conceptual model (Yoshioka et al., 2008). In this study, we built a geomechanical reservoir simulation based on the geologic model described in Section 2.

4.1 Simulation domain

As indicated in Figure 3, several clusters of open fractures were identified from logging and drilling fluid losses. The shallowest cluster can be found around 4350 ft MD. This depth coincides with the feedzone from the spinner survey. From the density of the open fractures, we chose two additional zones as a dominant feedzone, which are 6100 ft MD (zone with partial losses observed during drilling) and 7100 ft MD (3428 ft bsl). The dominant strike of open fractures in the known well permeable zone is approximately N±30°, consistent with surface structures (Stimac *et al.*, 2008; Stimac et al., 2010). Therefore, we consider multiple vertical fractures that intersect the deviated Awi 18-1 well in N-S direction at the 4350, 6100, and 7100 ft MD. For the dimension of the computation grid, we extended the vertical dimension for about 5000 ft below the well toe (about 9600 ft bsl) because the downward migration of microseismicity was observed (Wibowo and Nordquist, 2010). Figure 8 shows a schematic of the computation domain.

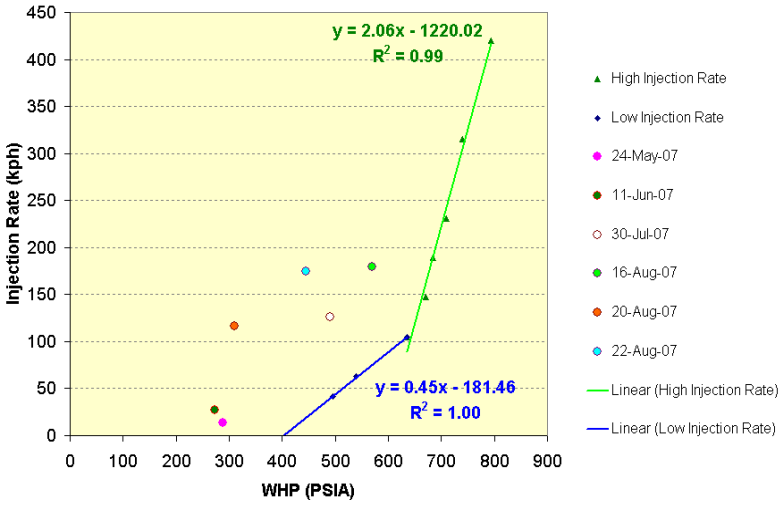

Figure 6: Injectivity after phase I stimulation.

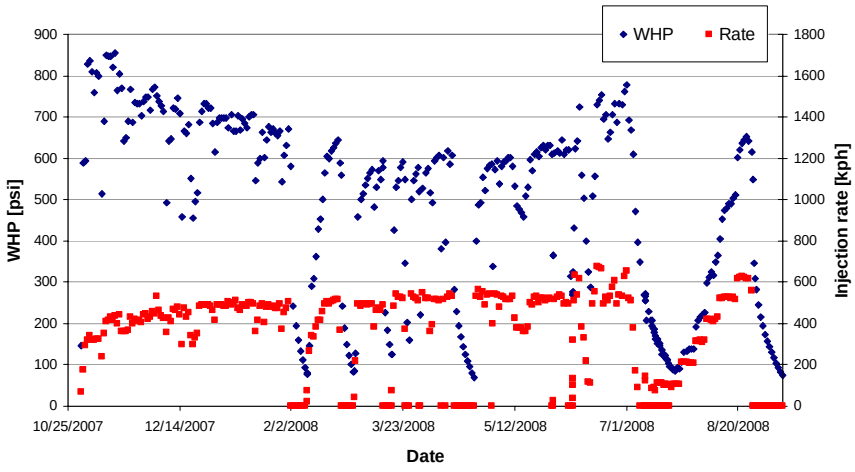

Figure 7: Injection history – phase II.

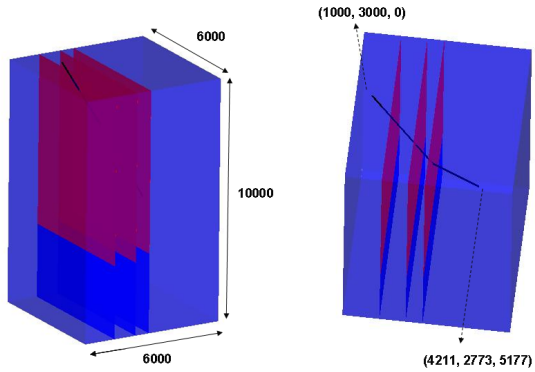

Figure 8: Schematic of the computation domain.

The formation top and rock properties of the area were estimated using the log data from the Awi 18-1 well, Rock Mechanics Analysis (RMA) log-based correlations for rock properties, and laboratory measurements on Awi 18-1 core. The log data are available up to the 7624 ft MD. Therefore, we do not have the information below this depth. Rock mechanical properties estimated are listed in Table 1. The properties for the unknown regions (3840 ft bsl) are assigned as the same as the last lithology (Dacite/Andesite). The numbers of cells in each formation are also given in Table 1 and Figure 9 shows the computational grid.

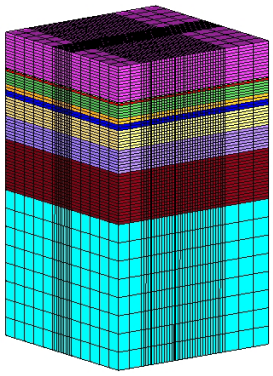

Figure 9: Computation grids and formation top.

4.2 Fracture conductivity

A relationship between fracture conductivity and applied stress has been studied extensively (Gangi 1978; Walsh 1981; Gale 1982; Swan 1983) and also equivalent hydraulic properties for continuum representation with multiple fractures have been investigated both analytically (Elsworth and Xiang 1989; Bai et al 1999; Liu et al. 1999; Zhang et al 2007) and numerically (Zhang et al 1996; Min et al 2004). Pressure dependent hydraulic conductivity models have been also successfully applied in several HDR projects (Zyvoloski 1985; Tenma *et al.* 2008).

The fractures the well intersects were assumed to be vertical considering the stress anisotropy in the field ($\sigma_v = 1.04$ psi/ft, $\sigma_H = 0.93$ psi/ft, $\sigma_h = 0.54$ psi/ft). The conductivities of the fractures were estimated as a function of stress and pore pressure by applying the Gangi's bed of nails model (Figure 10) as:

$$W = W_0\left[1-\left(\frac{\sigma - P}{E_{eff}}\right)^{1/n}\right] \tag{2}$$

where σ is the normal stress applied to the fracture face and P is the fracture pressure. E_{eff} is the effective Young's modulus defined as

$$E_{eff} = E\,A_r / A \tag{3}$$

where A is the area of the fracture face where the force, F, is applied and A_r is the area of nail surfaces. Letting the length of rod i be l_i and its area be a_i (Figure 10), A_r can be calculated as

$$A_r = \sum_{i=1}^{I_0} a_i n(l_i) \tag{4}$$

where I_0 is the total number of rods and $n(l_i)$ is the number of rod i. The assumptions made to derive the expression given in Eq. 1 are: the ratio a_i to l_i is constant and the distribution of rod's length is given by a power law,

$$N(x) = I_0 (x/w_0)^{n-1} \tag{5}$$

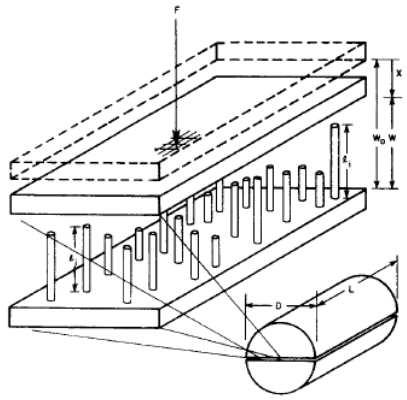

Figure 10: Bed of nails model (Gangi, 1978).

Once the width of the fracture is determined, we applied cubic law (Snow 1965) to calculate the fracture permeability as:

$$k = \frac{W^2}{12} \tag{6}$$

As we inject cold water into fracture system, the stress profiles of the field will deviate from the in-situ condition. As a consequence, a large region of tensile stress will be developed along the existing fracture planes. We consider the tensile failure criteria as

$$\sigma - p < T_0 \tag{7}$$

where T_0 is the tensile strength.

For the permeability estimation after tensile failure, we will apply the stress dependent permeability model for fractured media by Zhang *et al.* (2007). The permeability change due to the aperture increment as shown in Figure 11 is given by

$$k_k = k_{k0}\left[1+\frac{\Delta b_i}{b_i}+\frac{\Delta b_j}{b_j}\right] \tag{8}$$

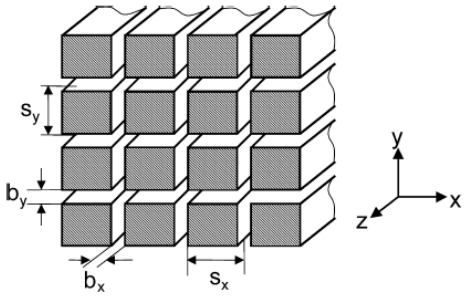

Figure 11: Fractured media with apertures (Zhang, 2008).

The displacement changes in each direction can be estimated by Hooke's law. Therefore, in terms of stress changes, and rock and fracture stiffness, Eq. 8can be rewritten as

$$k_k = k_{k0}\left\{1-\left(\frac{1}{K_{ni}}+\frac{b_i}{K_{ni}s_i}+\frac{b_i}{E_r}\right)\left[\Delta\sigma_i-\nu\left(\Delta\sigma_j+\Delta\sigma_k\right)\right]\right.$$
$$\left.-\left(\frac{1}{K_{nj}}+\frac{b_j}{K_{nj}s_j}+\frac{b_j}{E_r}\right)\left[\Delta\sigma_j-\nu\left(\Delta\sigma_i+\Delta\sigma_k\right)\right]\right\}^3 \quad (9)$$

Taking account into only the changes of the least stress, we have

$$k_k = k_{k0}\left[1-\left\{\left(\frac{1}{K_{ni}}+\frac{b_i}{K_{ni}s_i}+\frac{b_i}{E_r}\right)\right.\right.$$
$$\left.\left.+\left(\frac{1}{K_{nj}}+\frac{b_j}{K_{nj}s_j}+\frac{b_j}{E_r}\right)\nu\right\}\Delta\sigma_3\right]^3 \quad (10)$$

or simply

$$k_k = k_{k0}\left[1-\eta\Delta\sigma_3\right]^3 \quad (11)$$

where

$$\eta = \left(\frac{1}{K_{ni}}+\frac{b_i}{K_{ni}s_i}+\frac{b_i}{E_r}\right)+\left(\frac{1}{K_{nj}}+\frac{b_j}{K_{nj}s_j}+\frac{b_j}{E_r}\right)\nu \quad (12)$$

We define k_{k0} as the permeability of the media when tensile failure occurs, and the stress difference $\Delta\sigma_3$ is given by the difference between the current stress and the tensile strength.

From Eqs. 2 and 11, we have six calibration parameters (W_0, n, A_r/A k_{k0}, $\Delta\sigma_3$, and η) to be determined by matching the field injection history data.

4.3 History match

The injection rate and WHP data have been monitored continuously for the entire 300 days of injection history. As calibration parameters, we have the parameters controlling primary fracture conductivity changes (Eq. 2) and secondary fracture propagation (Eq. 11). Also, we need to specify the dimensions for the primary fractures.

The history match has been conducted manually by calibrating the parameters. Firstly, we have adjusted the parameters of the primary fractures and their dimensions, obeying the early period of the history because they are the dominant parameters in overall performance and early period before secondary fractures are developed. Since spinner data below 6100 ft are not available and we have no information on how much water is allocated to each feedzone below this depth, we treated each feedzone equally. In other words, we have used the same parameters for all primary fractures and also used the same dimensions while different rock mechanical properties are assigned accordingly in each formation. Therefore, each fracture will behave differently. After a rough overall pressure match, we started a calibration of detailed pressure data. The calibrated parameters and the initial primary fracture dimensions are listed in Table 2 and the final history match results are shown in Figure 12.

Table 2: Calibrated parameters and fracture dimensions.

n	10	***k0***	2500 md
A/Ar	0.1	***η***	0.0005 psi^{-1}
W_0	0.012 in	***T0***	200 psi
		Ly	1000 ft
		Lz	7000 ft

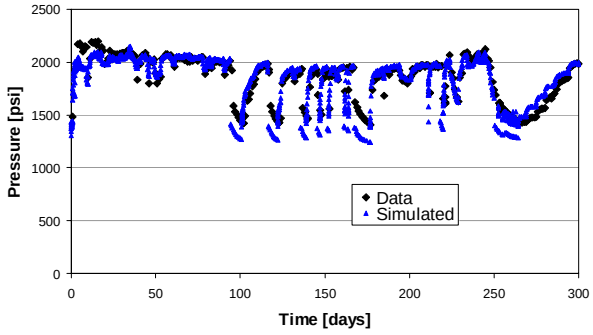

(a)

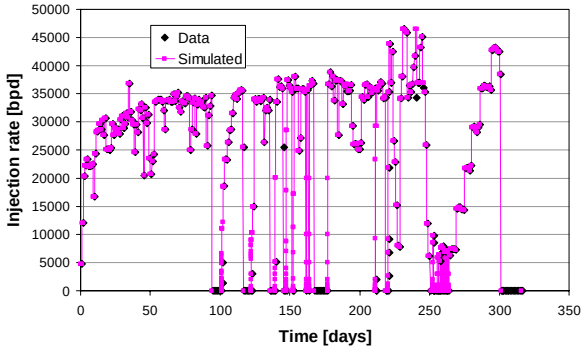

(b)

Figure 12: History match result (a) pressure and (b) injection rate.

The overall pressure history is matched quite well and captures most of the features of the history closely. However, the periods during the pressure fall off tests were not matched very well. This may be because the stress-

pressure dependent permeability models applied do not work well in the 'reverse' flow condition. This could be the reason we see more rapid fall-off in the simulation than the field observation. Despite the unmatched PFO, this close history match result gives us high confident with our calibration and the model should be representative of the injectivity evolution in reality.

The pressure profiles of *x* and *y* planes during the simulation are shown in Figure 13. The *x* plane is the location of the deepest feed zone (7100 ft MD) and contains the prescribed fracture (high permeability plane). Due to the well deviation and initial fracture dimension, the pressure profiles show asymmetric behavior. Figure 14 shows the temperature profiles. The temperature profiles are representative of the fluid flow. We can see from the figure that the water flows horizontally from the intersection of the wellbore and the fracture plane and the paths are derailed vertically due to the flow restriction by the initial fracture dimensions. The stresses will be reduced by cooling and the tensile failure criteria (Eq. 7) are met in some regions. Figure 15 shows the profiles of the stress in *x* direction. The reductions of the stress can be found near the wellbore initially and grow further in later time. The reductions show very close correlation with the cooled zones. Figure 16 shows the permeability multiplier profiles. As we observed in the stress or the temperature profile, the enhanced permeability region propagates mainly horizontally and vertically near the flow restrictions. The selectivity in horizontal direction is caused by different formation's mechanical properties. The enhanced permeability region is expanded as we inject water.

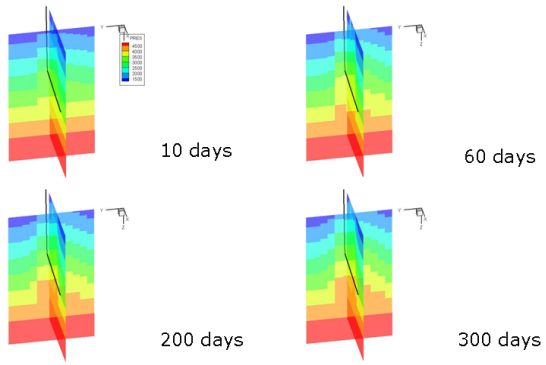

Figure 13: Pressure profiles.

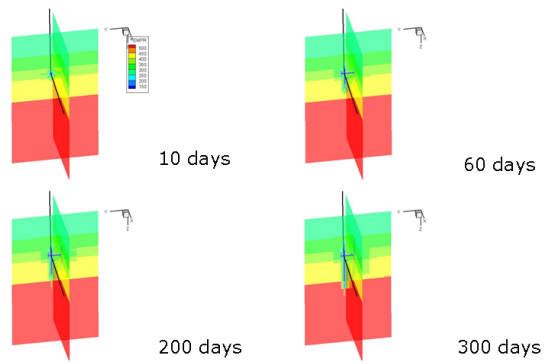

Figure 14: Temperature profiles.

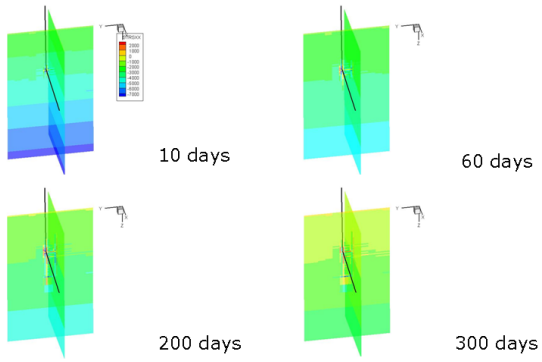

Figure 15: Stress (x-direction) profiles.

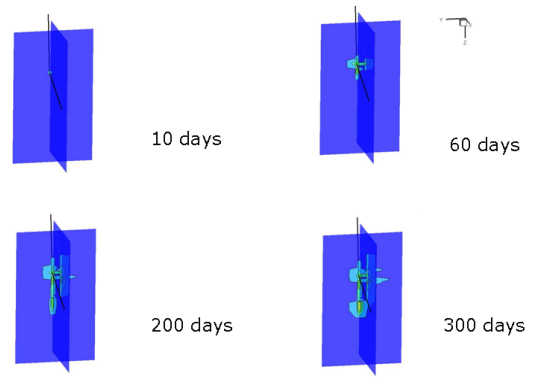

Figure 16: Permeability multiplier profiles.

5. OPTIMAL STIMULATION DESIGN

One of our main objectives is to understand the injectivity evolution mechanism and behavior during the hydraulic stimulation. The other objective of the study is to evaluate various possible operational scenarios for future injection performance. In this section, we run various what-if simulations based on different operation scenario and make recommended injection scheme for future Awi 18-1 use and other hydraulic stimulation in a similar situation.

5.1 Injection pressure

A pressure of 500 psi can be maintained from the sump gravity at the wellhead without using pumps. To investigate the efficiency, we simulated the future performances with the calibrated model considering 500 psi, 750 psi, and 1000 psi of wellhead pressure respectively. Figure 17 shows the injection efficiency (q/p_{wh}) of the three cases for comparison.

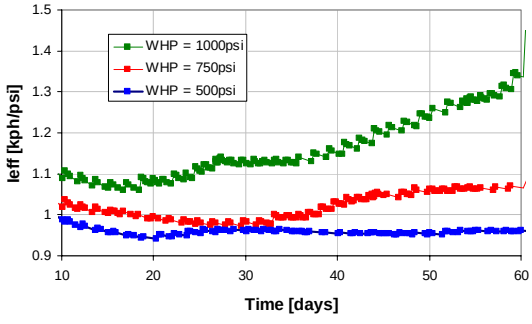

Figure 17: Future injection prediction of different wellhead pressures.

The injection efficiencies of wellhead pressure 500 psi and 750 psi are fairly close despite the additional energy dedicated for the 750 psi case. However, with the wellhead pressure of 1000 psi, it shows steadily higher injection efficiencies than other scenarios and it is projected to be increasing with time.

5.2 Injection temperature

As thermal contraction reduces the stresses of the earth, colder injectate can enhance the formation permeability more. During the hydraulic stimulation, we injected the condensate water from the power plant. To answer the question whether we need to keep utilizing condensate water, we compared the injection performances of injection temperature of 100°F, 220°F, and 340°F (Figure 18). The wellhead pressure was considered to be 500 psi.

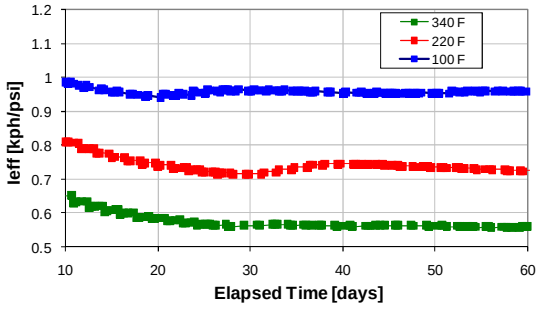

Figure 18: Future injection prediction of different injection temperature.

The comparison results clearly show the injection temperature effects. The colder injection temperature, the better injection efficiency can be achieved with the same wellhead pressure. It indicates that the cooler injectate can reduce the required wellhead pressure for water injection in the field.

5.3 Cycling pressure

In the field operation, we have observed injectivity improvement after the well shut-in. This observation led us to the pressure cycling injection. Although we saw some improvements, the results are not consistent. In this example, we simulated cycling pressure injection (well shut-in every 10 days). The results are shown and compared with the normal injection (WHP=500 psi) in Figure 19.

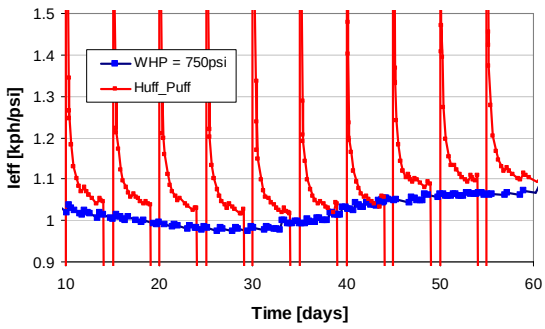

Figure 19: Future injection prediction of cycling pressure injection.

Cycling pressure injection seems to perform a little better from the figure. However, it is hard to draw any conclusions from this small increase. The geomechanical simulation of this study applied stress dependent permeability regarding a fractured rock mass as continuum material. It may require more detailed study to address cycling pressure injection effects.

5.4 Cycling temperature

As a last examination, we run scenarios of cycling temperature case to see if any additional effects on the injection efficiency. Cycling injection temperature is not impossible from operation stand point but it would be costly. Therefore, the scenario should be strongly supported by successful concept. Figure 20 shows the simulation comparing results from cycling temperature (220°F and 340°F). A cycling temperature from 220°F to 340°F does not outperform the injection operation with 220°F constant injection temperature and shows even lower performance (Figure 20).

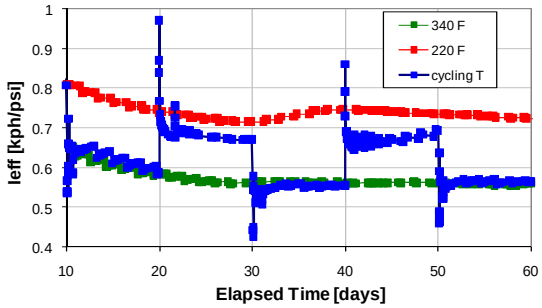

Figure 20: Future injection prediction of cycling temperature injection.

6. CONCLUSIONS

In this study we developed a 3-D geomechanical reservoir simulation model of a deviated injector Awi 18-1, which contains prescribed fracture planes identified from PTS and image logs. In the simulation, injectivity evolution mechanisms are considered to be two folds: 1) hydraulically dilating existing fracture apertures, and 2) creating tensile fractures (thermal cracking or spalling) from the existing fractures. The developed model was successfully calibrated against the field history and a number of what-if operational scenarios were run. From the simulation, we can draw following conclusions:

- The higher injection pressure or the colder injection temperature, the better injection efficiency. Created fractured volume would be simply proportional to the injected volume and the cooled formation volume, whose stresses are reduced from the in-situ.
- Cycling pressure or temperature does not outperform the injection operation with the highest pressure or coolest temperature all the way through at the end.

7. ACKNOWLEDGEMENTS

The authors thank Chevron for permission to publish the study and their colleagues for fruitful discussions. Special thanks also go to Horasdo Pasaribu, Terry Indra, Nurlianto Sadji, Rudy Sophian, and Noor Rosyadi of Chevron for maintaining the safe and reliable operations at the site.

REFERENCES

Bai, M., Meng, F., Elsworth, D., and Roegiers, J.-C.: "Analysis of Stress-Dependent Permeability in

Nonorthogonal Flow and Deformation Fields," Rock Mechanics and Rock Engineering (1999), 195-219.

Elsworth, D., and Xiang, J.: "A Reduced Degree of Freedom Model for Thermal Permeability Enhancement in Blocky Rock," Geothermics (1989), 691-709.

Gale, J.E.: "The Effects of Fracture Type (Induced versus Natural) on the Stress-Fracture Closure-Fracture Permeability Relationships," Proc., 23rd U.S. Symp. on Rock Mechanics, Berkeley, CA, (1982), 290-298.

Gangi, A.F.: "Variation of Whole and Fractured Porous Rock Permeability with Confining Pressure," Int. J. of Rock Mechanics Mining and Geomechanical Abstracts (1978), 249-257.

Liu, J., Elsworth, D., and Brady, B.H.: "Linking Stress-Dependent Effective Porosity and Hydraulic Conductivity Fields to RMR," Int. J. Rock Mechanics and Mining Sciences (1999), 581-596.

Min, K.-B., Rutqvist, J., Tsang, C.-F., and Jing, L.: "Stress-Dependent Permeability of Fractured Rock Masses; A Numerical Study," Int. J. or Rock Mechanics and Mining Sciences (2004), 1191-1210.

Snow, D.: "A Parallel Plate Model of Fractured Permeable Media," PhD Dissertation, University of California, Berkeley, CA, 1965.

Stietel, A., et al.: "Continuum Representation of Coupled Hydromechanic Processes of Fractured Media: Homogenisation and Parameter Identification," Coupled Thermo-Hydro-Mechanical Processes of Fractured Media (1996), Elsevier, Amsterdam.

Stimac, J., Baroek, M., Suminar, A., and Sagala, B.: Integration of surface and well data to determine volcanic and structural controls on permeability at Awibengkok (Salak), Indonesia. Proceedings, WGC2010, Bali, Indonesia.

Stimac, J., Nordquist, G., Suminar, A., and Sirad-Azwar, L.: An overview of the Awibengkok geothermal system, Indonesia, *Geothermics* **37**, (2008), 300-331.

Sugiaman, F.: State of stress and wellbore stability in Awibenkgok field. Unpublished Unocal report. (2003).

Swan, G.: "Determination of Stiffness and Other Joint Properties from Roughness Measurements," Rock Mechanics and Rock Engineering (1983), 19-38.

Tenma, N., Yamaguchi, T., and Zyvoloski, G.: "The Hijiori Hot Dry Rock Test Site, Japan Evaluation and Optimization of Heat Extraction from a Two-layered Reservoir," Geothermics (January 2008), 19-52.

Walsh, J.B., and Grosenbaugh, M.A.: "New model for analyzing the effect of fractures on compressibility," Journal of Geophysical Research (1979), 3532-3536.

Wobowo, D., and Nordquist, G.: Microseismicity associated with hydraulic stimulation of Awi 18-1, Salak, Indonesia. Proceedings WCG2010 (Bali).

Yoshioka, K., Izgec, B., and Pasikki, R.: Optimization of geothermal well stimulation design using a geomechanical reservoir simulator, *Proceedings*, 33rd Workshop on Geothermal Reservoir Engineering, Stanford University, Stanford, CA (2008).

Yoshioka, K., Pasikki, R., Suryata, I., and Riedel, K.: Hydraulic Stimulation Techniques Applied to Injection Wells at the Salak Geothermal Field Indonesia, paper SPE 121184, presented at the 2009 SPE Western Regional Meeting, San Jose, CA, 24-26 March.

Zhang, X, Sanderson, D.J., Harkness, R.M., and Last, N.C.: "Evaluation of the 2-D Permeability Tensor for Fractured Rock Masses," Int. J. of Rock Mechanics Mining and Geomechanical Abstracts (1996), 17-37.

Zhang, J., Standifird, W.B., Roegiers, J.C., and Zhang, Y.: "Stress-Dependent Fluid Flow and Permeability in Fractured Media: from Lab Experiments to Engineering Applications," Rock Mechanics and Rock Engineering (2007), 3-21.

Zyvoloski, G.: "The Sizing of a Hot Dry Rock Reservoir from a Hydraulic Fracturing Experiment," presented at the 26th US Symposium on Rock Mechanics, Rapid City, SD, 26 – 28 Jun, 1985.